A Sensitive UV Photodetector Based on Non-Wide Bandgap $MAPbBr_3$ Nanosheet

Ming-Ming Liu, Liang-Liang Zhou, Shi-Fu Li, Feng-Xia Liang, Yue Xing, Jing-Yue Li, Can Fu, Yao-Zu Zhao, Di Wu, and Lin-Bao Luo, *Senior Member, IEEE*

***Abstract*— A sensitive ultraviolet photodetector (UVPD) based on an ultrathin $MAPbBr_3$ nanosheet was developed in this study. A simulation based on technology computer-aided design showed that the optical absorption of $MAPbBr_3$ can be tailored by changing the material thickness, which is reasonable considering the wavelength dependence of the absorption coefficient of $MAPbBr_3$. In addition, an apparent blueshift of the position of the maximum photocurrent is observed upon decreasing the nanosheet thickness. These tunable optoelectronic properties resulted in a device fabricated from medium-bandgap 43-nm-thick $MAPbBr_3$ nanosheets being sensitive to UV light illumination. The device has a maximum photoresponse at 300 nm, a responsivity of 27.2 $mA{\cdot}W^{-1}$, and a response speed of 0.103/0.087 s, respectively, which are comparable to conventional UVPDs based on low-dimensional wide bandgap materials (e.g., ZnO and TiO_2). This novel UVPD has application potential to optoelectronic systems.**

***Index Terms*— Optical absorption, perovskite, ultrathin nanosheet, ultraviolet photodetector (UVPD).**

I. Introduction

HIGH-PERFORMANCE ultraviolet photodetectors (UVPDs) made of wide bandgap semiconductors (SiC [1], GaN [2], Ga_2O_3 [3], etc.) are widely used in various military and civilian fields. However, the application of these materials is hindered by inevitable drawbacks, such as relatively harsh preparation conditions and high manufacturing costs [4]. Recently, rapid advances in nanofabrication have motivated an increasing number of research studies on novel UVPDs composed of narrow bandgap semiconductors. For instance, Xu *et al.* recently reported a novel UVPD consisting of graphene combined with ultrathin silicon. The as-fabricated device displayed a sensitive response to 365-nm light, a high photoresponse of 0.47 $A{\cdot}W^{-1}$, and superior mechanical flexibility [5]. The aforementioned intriguing study demonstrated that anomalous optoelectric properties can be realized by intentionally adjusting the optical property of Si, thereby providing a novel route for fabricating UVPDs from narrow-bandgap materials.

Organic-inorganic hybrid perovskites have been demonstrated to have considerable potential for various optoelectronic applications due to good solution processability and a low cost, as well as excellent optoelectronic properties, including tunable bandgaps, large absorption coefficients, and long carrier diffusion lengths [6]–[8]. Among organic-inorganic hybrid perovskites, $MAPbI_3$, $MAPbBr_3$, and $MAPbCl_3$ are the most studied and have bandgaps of approximately 1.5, 2.2, and 3.1 eV, with corresponding absorption edges in the near infrared (NIR), visible (VIS), and UV ranges, respectively. To date, many groups have tried to widen the response range of these materials by bandgap engineering. Impressive progress has consequently been made in the fabrication of excellent VIS light-absorbing materials for VIS-light detection [9], [10]. However, to the best of our knowledge, very few perovskite-based UV methods have been reported, except for rare devices composed of wide bandgap hybrid perovskites (e.g., $MAPbCl_3$ [11] and MA_2MnCl_4 [12]).

Inspired by the aforementioned studies, we developed a sensitive UVPD by using a nonwide bandgap $MAPbBr_3$ nanosheet as a building block. Theoretical simulations showed that the response peak of the $MAPbBr_3$-based PD can be readily tuned, which is reasonable as the absorption coefficient depends on the wavelength of incident light. Moreover, the maximum photoresponse of the PD can be shifted to short wavelengths by reducing the thickness of the nanosheets. Notably, a UVPD made of 43-nm-thick perovskite nanosheets exhibits typical UV sensitivity with a peak at approximately 300 nm. The responsivity and specific detectivity were estimated to be 27.2 $mA{\cdot}W^{-1}$ and 6.38 $\times$ 10^8 Jones, respectively, which are comparable to previously reported UVPDs composed of traditional wide bandgap semiconductor materials.

II. Experiments

A. Materials Synthesis

$MAPbBr_3$ nanosheets were grown on a mica substrate using a previously reported confined-space method [13]. First, a

Manuscript received 10 June 2022; revised 19 July 2022 and 27 July 2022; accepted 28 July 2022. This work was supported in part by the National Natural Science Foundation of China under Grant 62074048, in part by the Key Research and Development Plan of Anhui Province under Grant 2022f04020007, in part by the Natural Science Foundation of Anhui Province under Grant 2208085MF177, and in part by the Fundamental Research Funds for the Central Universities under Grant PA2020GDKC0014 and Grant JZ2018HGXC0001. The review of this article was arranged by Editor J. D. Phillips. *(Corresponding author: Lin-Bao Luo.)*

Ming-Ming Liu, Liang-Liang Zhou, Shi-Fu Li, and Yao-Zu Zhao are with the Anhui Provincial Key Laboratory of Advanced Functional Materials and Devices, School of Materials Science and Engineering, Hefei University of Technology, Hefei 230009, China.

Feng-Xia Liang, Yue Xing, Jing-Yue Li, Can Fu, and Lin-Bao Luo are with the School of Microelectronics, Hefei University of Technology, Hefei 230009, China (e-mail: fxliang@hfut.edu.cn; luolb@hfut.edu.cn).

Di Wu is with the Key Laboratory of Material Physics of Ministry of Education, School of Physics and Engineering, Zhengzhou University, Zhengzhou, Henan 450052, China.

Color versions of one or more figures in this article are available at https://doi.org/10.1109/TED.2022.3195689.

Digital Object Identifier 10.1109/TED.2022.3195689

$MAPbBr_3$ perovskite precursor was prepared. MABr (Xian Polymer Light Technology Company, Ltd., 99.5%) and $PbBr_2$ (Macklin, 99%) were dissolved in N, N-dimethylformamide (DMF, 99.5%) in a 1:1 mole ratio. The solution was stirred for 2 h at 40 °C and then passed through a polytetrafluoroethylene filter. Next, a mica sheet was cleaved in the middle into two pieces; 5 μL of the $MAPbBr_3$ precursor solution was dropped onto one mica sheet and promptly covered with the other mica sheet. Finally, the mica sheets were placed on a hotplate and heated at 30 °C under an appropriate pressure for more than 12 h. The thickness of the $MAPbBr_3$ sheet could be tailored by adjusting the solution concentration and heating temperature.

B. Device Fabrication and Characterization

To fabricate the $MAPbBr_3$-based PD, two 50-nm-thick Au electrodes were deposited on a $MAPbBr_3$ nanosheet using a homemade shadow mask by an e-beam evaporator. The channel width was 20 μm. A semiconductor characterization system (Keithley 2400-SCS) with a broadband monochromator (SP 2150, Princeton Company) was used to study the opto-electronic characteristics of the as-fabricated PD. In addition, laser diodes of various wavelengths were employed (Thorlabs 265, 300, 365, 450, 530, and 660 nm). The power intensities of all the diodes were calibrated using a power meter (Thorlabs GmbH, PM 100D) before performing measurements.

The morphology of the as-synthesized nanosheets was characterized by an optical microscope (MV 300), field-emission SEM (Regulus 8230), and atomic force microscopy (AFM, Dimension Icon). The phase composition of the nanosheets was determined using an X-ray diffractometer (X'Pert PRO MPD).

C. Theoretical Simulation

Technology computer aided design (TCAD) software was used to simulate the light-intensity attenuation of the perovskite material. The intensity, angle, and position of the illuminated light were designed to simulate the photoelectric behavior of the devices. The simulated results were used in conjunction with the contour drawing component of the software to present the spectra for the evolution of light intensity in different colors.

III. Results and Discussion

A simple PD with a typical photoconductive-type geometry was fabricated by using $MAPbBr_3$ nanosheet. A detailed schematic of the device is shown in Fig. 1(a). Briefly, nanosheets were synthesized by a previously reported confined-space method employing mica as a group substrate. Then, a simple PD with a channel width of 20 μm was constructed by depositing two parallel Au electrodes on the as-synthesized nanosheet. Fig. 1(b) shows the XRD spectra of a $MAPbBr_3$ nanosheet on a mica substrate. The diffraction peaks at 15.2°, 30.4°, and 46.1° clearly correspond to the (100), (200), and (300) lattice planes of cubic $MAPbBr_3$ [14], [15]. Fig. 1(c) shows the optical and SEM images of a typical $MAPbBr_3$ nanosheet with a side length of approximately 91 μm and a thickness of 59 nm. Subsequent AFM analysis

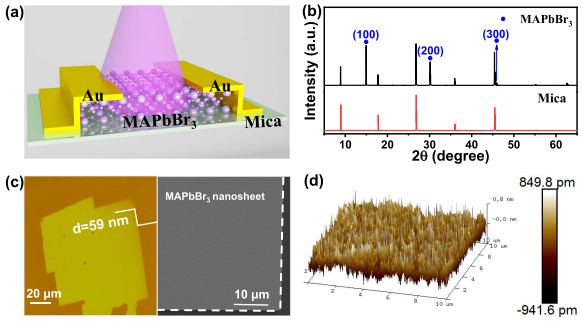

Fig. 1. (a) Schematic of the fabricated $MAPbBr_3$ nanosheet PD. (b) XRD spectra of a $MAPbBr_3$ sample on a mica substrate and a bare mica substrate. (c) Typical optical and SEM images of a $MAPbBr_3$ nanosheet on mica. (d) Tapping-mode AFM height profile of the $MAPbBr_3$ nanosheet.

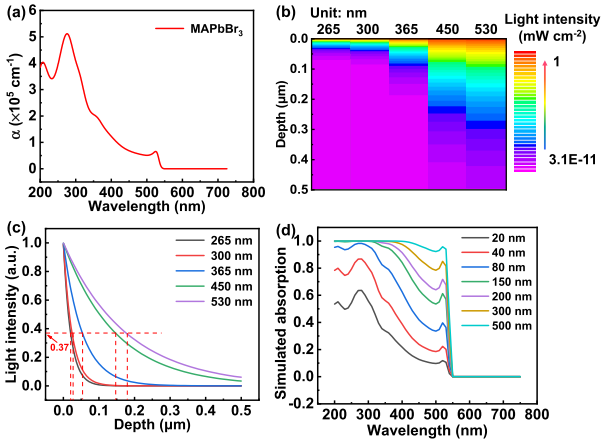

Fig. 2. (a) $MAPbBr_3$ absorption coefficient. (b) Light-intensity attenuation versus the depth and (c) normalized attenuation curve. (d) Simulated absorption curves of $MAPbBr_3$ nanosheets of different thicknesses.

showed that the nanosheet had a relatively good surface roughness [see Fig. 1(d)], with an arithmetic mean roughness (Ra) and root mean square roughness (Rq) of 0.193 and 0.257 nm, respectively.

The fabricated $MAPbBr_3$ has a medium bandgap but can nevertheless be used to prepare a UVPD because the optical property of a perovskite nanosheet is determined by both the absorption coefficient and the thickness. The absorption coefficient (α) of $MAPbBr_3$ was calculated by employing the wavelength-dependent (λ) extinction coefficient (k) [16]–[18]

$$\alpha = \frac{4\pi k}{\lambda}. \tag{1}$$

Fig. 2(a) shows the absorption coefficient as a function of the incident wavelengths. The absorption coefficient clearly drops gradually as the wavelength increases, e.g., from 4.07×10^5 cm^{-1} at 300 nm to approximately 5.64×10^4 cm^{-1} at 530 nm, which is consistent with the results of a previous study [17], [18]. This wavelength-dependent absorption coefficient results in a distinct photon absorption when light of different wavelengths shines on the material, as shown by the results of the theoretical simulation implemented using TCAD [see Fig. 2(b)].

Note that in the simulation, the perovskite thickness was approximately 0.5 μm, and the initial light intensity was set to 1 $mW{\cdot}cm^{-2}$ for all simulated wavelengths. Apparently, light with a short wavelength decays relatively faster than light

with a long wavelength. For instance, at a depth of 100 nm, the intensity of 300-nm UV illumination drops sharply to approximately 7.8×10^{-3} mW·cm^{-2}, whereas the intensity of the 530-nm VIS light only decreases to approximately 5.6×10^{-1} mW·cm^{-2}, which is reasonable considering the relatively lower absorption coefficient for long-wavelength light. Fig. 2(c) is a quantitative plot of the gradual decline in the light intensity with increasing depth for different wavelengths. The penetration depth marked in the curve clearly decreases with decreasing wavelength. Specifically, the penetration depth decreases from approximately 177.4 nm for 530-nm light to 24.5 nm for 300-nm UV light. This wavelength-dependent penetration depth increases absorption in the UV region. Fig. 2(d) shows that the simulated absorption varies with the nanosheet thickness, both in terms of the intensity and position of the maximum absorption. Specifically, broadband absorption from 260 to 550 nm occurs for $MAPbBr_3$ with a thickness of approximately 500 nm, for which the optical absorption characteristics were similar to those reported for the bulk material [19]. However, a gradual reduction in the thickness produces a clear decrease in photoabsorption over the entire UV-visible region because a thin film has a limited absorption cross section. Further careful analysis showed that the light absorption of long-wavelength illumination decreases more rapidly than that of short-wavelength illumination, such that UV absorption is dominant for small nanosheet thicknesses.

To determine the effect of the thickness on the optoelectronic property of $MAPbBr_3$ nanosheet, the photocurrent was further studied through TCAD simulation. Fig. 3(a) is a comparison of the normalized photocurrents at a 3-V bias of a variety of PDs, which are composed of $MAPbBr_3$ nanosheets with thicknesses ranging from 20 to 500 nm. A similar trend to that for photoabsorption can be observed in the evolution of the photocurrent, which is reasonable considering that the photocurrent of a photoconductive PD is mainly formed through the separation of photogenerated carriers under an external electric field. Moreover, the maximum response peak of the photocurrent blueshifts from 530 to 280 nm as the thickness decreases from 500 to 20 nm. Note that the 530-nm peak is mainly attributed to band edge absorption of $MAPbBr_3$ [20], [21]. The corresponding UV/visible (R_{300}/R_{450}) rejection ratio calculated using data extracted from Fig. 3(a) increases from 0.69 to 2.92 as the thickness of $MAPbBr_3$ decreases [see the inset of Fig. 3(a)]. The rejection ratio R_{300}/R_{450} is not high but nevertheless presents a feasible route to realize a UVPD. Material studies have shown that increasing the absorption coefficient in the UV region over that in the VIS region, decreasing the thickness, and using a high-quality surface with few defects typically increase the UV-to-VIS rejection ratio [5], [22], [23]. $MAPbBr_3$ nanosheets of three different thicknesses (43, 75, and 366 nm) were synthesized by varying the solution concentration, and corresponding devices labeled PD1, PD2, and PD3 were fabricated. Fig. 3(b) is a comparison of the normalized photoresponses of the three PDs under illuminations of different wavelengths (i.e., 265, 300, 365, 450, 530, and 660 nm) at a 3-V bias. The three PDs clearly exhibit different maximum photoresponses, which are 300 nm for PD1, 365 nm for PD2, and 530 nm for PD3, which

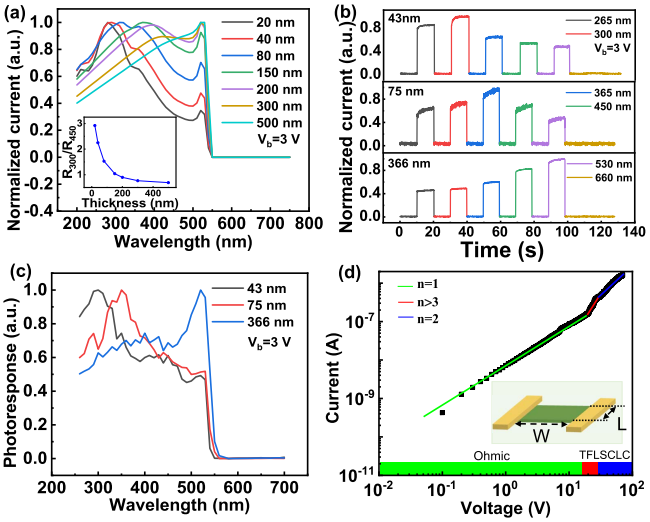

Fig. 3. (a) Normalized simulated current curve of $MAPbBr_3$ nanosheet PDs of different thicknesses. The inset shows the rejection ratios R_{300}/R_{450} for nanosheets of different thicknesses. (b) Normalized $I-T$ curves obtained under illumination of various wavelengths. (c) Normalized photoresponse of devices based on nanosheets of different thicknesses. (d) SCLC measurement of a $MAPbBr_3$ nanosheet. The inset is a schematic of the device structure used in the measurement.

is consistent with the normalized spectral response shown in Fig. 3(c). Furthermore, to quantitatively study the electrical properties of the materials, the trap density and mobility of the as-synthesized nanosheet were investigated by the commonly used space charge limited current method (SCLC) [24]–[26]. A gap-type structured device, which is illustrated in the inset of Fig. 3(d), was prepared by evaporating two Au electrodes on the nanosheet [14], [26], [27]. Fig. 3(d) shows three typical regions in the corresponding current–voltage ($I-V$) curve measured under dark conditions: ohmic (green); trap-filling (red), starting at $V_{\mathrm{TFL}} = 20$ V; and SCLC (blue). The trap density for operation in the trap-filling region was obtained using the formula

$$n_{\mathrm{trap}} = \frac{2\varepsilon_0 \varepsilon V_{\mathrm{TFL}}}{eL^2} \tag{2}$$

where ε_0 is the vacuum permittivity ($\varepsilon_0 = 8.85 \times 10^{-14}$ F·cm^{-1}), ε is the relative dielectric constant ($\varepsilon = 4.8$), e is the elementary charge, and L is the electrode distance ($L = 58$ μm). The SCLC region can generally be described by Geurst's SCLC model

$$I = \frac{2\mu\varepsilon_0\varepsilon W V^2}{\pi L^2} \tag{3}$$

where μ is the carrier mobility, V is the applied voltage ($V = 29$ V), and W is the gap width of the electrode ($W = 20$ μm). The trap density and carrier mobility were estimated to be 3.1×10^{12} cm^{-3} and 31 cm^2·V^{-1}·s^{-1}, respectively, which are slightly higher than those of polycrystalline perovskite films [28], [29].

Finally, optoelectronic performance of the UV sensitive PD1 composed of a 43-nm-thick sheet was studied. Fig. 4(a) shows the $I-V$ curves of the PD obtained under different light intensities with a wavelength of 300 nm. The photocurrent clearly increases monotonically as the light intensity increases from 0.022 to 0.607 mW·cm^{-2}. This increase in

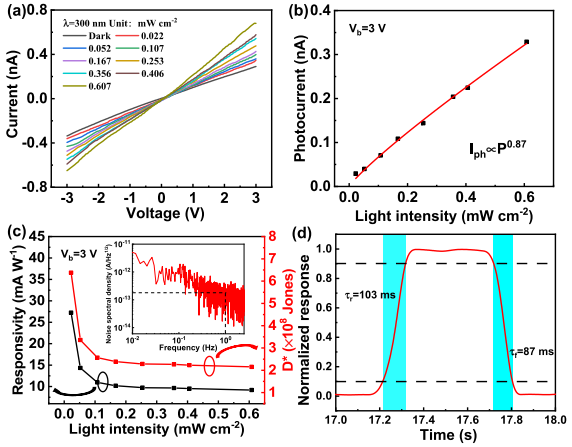

Fig. 4. (a) Current–voltage (I–V) curves of PD1 under 300-nm illumination with different light intensities. (b) Fitted relationship between the photocurrent and intensity for 300-nm illumination. (c) Responsivity and specific detectivity as a function of the light intensity for 300-nm illumination. The inset shows the noise spectral density obtained from an FFT of the dark current. (d) Single magnified photoresponse cycle for determining the rise/fall time for 300-nm illumination.

the photocurrent could be attributed to the creation of more carriers at higher intensities [30]. Furthermore, a general power law was employed to describe the relationship between the photocurrent and light intensity [31]

$$I_{\text{ph}} = P^{\theta} \tag{4}$$

where I_{ph}, P, and θ denote the net photocurrent, light intensity, and an empirical constant that accounts for carrier recombination, respectively. Fig. 4(b) shows that $\theta = 0.87$, which is smaller than 1 and implies that a loss is incurred due to recombination activity during the complex photodetection process. Subsequently, the main parameters of the responsivity (R) and specific detectivity (D^*) were calculated using the following equations [32]–[34]:

$$R = \frac{I_{\text{ph}}}{PS} \tag{5}$$

$$NEP = \frac{\overline{i_n^2}^{1/2}}{R} \tag{6}$$

$$D^* = \frac{(S\Delta f)^{1/2}}{NEP} \tag{7}$$

where S, P, Δf, $\overline{i_n^2}^{1/2}$, and NEP denote the effective area of the device, incident light intensity, specific bandwidth, root-mean-square value of the noise current, and noise equivalent power, respectively. The noise level of $\overline{i_n^2}^{1/2}$ at 1-Hz bandwidth was deduced to be 3.01×10^{-13} A/Hz$^{1/2}$ based on a fast Fourier transform (FFT) of the noise current [see the inset of Fig. 4(c)]. In Fig. 4(c), both R and D^* decrease as the incident light intensity increases, showing that increased charge carrier scattering induced by self-heating and recombination may occur at high intensities [3]. In addition, a maximum R and D^* of 27.2 mA·W^{-1} and 6.38×10^8 Jones are achieved at the lowest light intensity of 0.022 mW·cm^{-2}.

Fig. 4(d) shows the rise and fall times of the as-fabricated device, which are estimated from a single photoresponse cycle to be 103 and 87 ms, respectively. Table I is a summary of the device performances of the developed nanosheet-UVPD and other low-dimensional wide bandgap UVPDs [35]–[46]. The main parameters of the developed nanosheet-UVPD are generally lower than some devices based on low-dimensional wide bandgap materials (e.g., GaN, SiC, and AlGaN). However, compared to TiO_2 or ZnO-based UVPDs, the developed nanosheet-UVPD has parameters that are comparable or even superior, a relatively lower specific detectivity, and a more competitive responsivity and response speed.

TABLE I
PERFORMANCE COMPARISON WITH UVPDS BASED ON TYPICAL WIDE BANDGAP MATERIALS

Material	Structure	Bias (V)	R (A/W)	D* (Jones)	τ_r/τ_f (s)	Refs
ZnO	NWs	2	0.46	-	-/4	35
	NRs	5	2.07×10^{-6}	2.2×10^{8}	18/13	36
	NPs	1	0.006	1.1×10^{7}	8.76/18.13	37
TiO_2	NRs	0	0.0013	5.92×10^{11}	-	38
	NRs	-1	0.01	-	1.4/6.1	39
	NTs	10	0.015	5.7×10^{10}	-	40
GaN	Thin film	5	0.23	-	-	41
	Thin film	5	0.34	1.24×10^{9}	0.28/0.45	42
SiC	Thin film	20	0.03	-	5.94×10^{-4} /6.99×10^{-1}	43
	NWs	0	0.17	7.2×10^{10}	-	44
AlGaN	Thin film	0	0.136	-	-	45
	Thin film	0	0.211	2.4×10^{13}	-	46
$MAPbBr_3$	NS	3	0.027	6.38×10^{8}	0.103/ 0.087	This work

NW, NP, NR, NT, and NS represent nanowire, nanoparticle, nanorod, nanotube, and nanosheet, respectively.

IV. CONCLUSION

In summary, we successfully constructed a sensitive UVPD based on a thin $MAPbBr_3$ nanosheet. TCAD simulations showed that the optical absorption properties of $MAPbBr_3$ can be tailored by varying the nanosheet thickness. Experimental characterization of various $MAPbBr_3$ devices of different thicknesses (43, 75, and 366 nm) showed that the maximum photocurrent position shifts from longer to shorter wavelengths as the thickness decreases. Specifically, a PD made of 43-nm-thick nanosheets exhibits a peak photoresponse at 300 nm. The corresponding responsivity and specific detectivity of the UVPD were estimated to be 27.2 mA·W^{-1} and 6.38×10^8 Jones, respectively. The proposed method is also applicable to the fabrication of other nonwide-bandgap semiconductor-based sensitive UVPDs, as long as there are large differences among the absorption coefficients for various wavelengths.

REFERENCES

[1] T. Yang *et al.*, "High-performance SiC nanobelt photodetectors with long-term stability against 300 °C up to 180 days," *Adv. Funct. Mater.*, vol. 29, no. 11, Dec. 2018, Art. no. 1806250, doi: 10.1002/ADFM.201806250.

[2] M. Spies *et al.*, "Bias-controlled spectral response in GaN/AlN single-nanowire ultraviolet photodetectors," *Nano Lett.*, vol. 17, no. 7, pp. 4231–4239, Jul. 2017, doi: 10.1021/acs.nanolett.7b01118.

[3] W.-Y. Kong *et al.*, "Graphene-β-Ga_2O_3 heterojunction for highly sensitive deep UV photodetector application," *Adv. Mater.*, vol. 28, no. 48, pp. 10725–10731, Oct. 2016, doi: 10.1002/ADMA.201604049.

[4] C. Xie *et al.*, "Recent progress in solar-blind deep-ultraviolet photodetectors based on inorganic ultrawide bandgap semiconductors," *Adv. Funct. Mater.*, vol. 29, no. 9, Jan. 2019, Art. no. 1806006, doi: 10.1002/ADFM.201806006.

[5] A. Ali *et al.*, "High-performance, flexible graphene/ultra-thin silicon ultra-violet image sensor," in *IEDM Tech. Dig.*, Dec. 2017, pp. 8.6.1–8.6.4, doi: 10.1109/IEDM.2017.8268354.

[6] C. Xie, C. Liu, H. Loi, and F. Yan, "Perovskite-based phototransistors and hybrid photodetectors," *Adv. Funct. Mater.*, vol. 30, no. 20, May 2020, Art. no. 1903907, doi: 10.1002/ADFM.201903907.

[7] H. Wang, S. Li, X. Liu, Z. Shi, X. Fang, and J. He, "Low-dimensional metal halide perovskite photodetectors," *Adv. Mater.*, vol. 33, no. 7, Feb. 2021, Art. no. 2003309, doi: 10.1002/ADMA.202003309.

[8] W. Tian, H. Zhou, and L. Li, "Hybrid organic-inorganic perovskite photodetectors," *Small*, vol. 13, no. 41, Sep. 2017, Art. no. 1702107, doi: 10.1002/SMLL.201702107.

[9] R. Dong *et al.*, "High-gain and low-driving-voltage photodetectors based on organolead triiodide perovskites," *Adv. Mater.*, vol. 27, pp. 1912–1918, Mar. 2015, doi: 10.1002/ADMA.201405116.

[10] Y. Fang and J. Huang, "Resolving weak light of sub-picowatt per square centimeter by hybrid perovskite photodetectors enabled by noise reduction," *Adv. Mater.*, vol. 27, no. 17, pp. 2804–2810, 2015, doi: 10.1002/ADMA.201500099.

[11] V. Adinolfi *et al.*, "Fast and sensitive solution-processed visible-blind perovskite UV photodetectors," *Adv. Mater.*, vol. 28, no. 33, pp. 7264–7268, Jun. 2016, doi: 10.1002/ADMA.201601196.

[12] Z. Nie *et al.*, "Layered and Pb-free organic–inorganic perovskite materials for ultraviolet photoresponse: (010)-oriented $(CH_3NH_3)_2MnCl_4$ thin film," *ACS Appl. Mater. Interfaces*, vol. 8, no. 41, pp. 28187–28193, Oct. 2016, doi: 10.1021/ACSAMI.6B08962.

[13] R. Wang *et al.*, "Facilitating all-inorganic halide perovskites fabrication in confined-space deposition," *Small Methods*, vol. 4, no. 7, Apr. 2020, Art. no. 2000102, doi: 10.1002/SMTD.202000102.

[14] T. Kim *et al.*, "Confined growth of high-quality single-crystal $MAPbBr_3$ by inverse temperature crystallization for photovoltaic applications," *Electron. Mater. Lett.*, vol. 17, no. 4, pp. 347–354, Apr. 2021, doi: 10.1007/S13391-021-00288-7.

[15] X. Wang *et al.*, "Asymmetrical photodetection response of methylammonium lead bromide perovskite single crystal," *Cryst. Res. Technol.*, vol. 52, no. 9, Sep. 2017, Art. no. 1700115, doi: 10.1002/CRAT.201700115.

[16] F. Liang *et al.*, "Highly sensitive ultraviolet and visible wavelength sensor composed of two identical perovskite nanofilm photodetectors," *Small*, vol. 17, no. 40, Aug. 2021, Art. no. 2102987, doi: 10.1002/SMLL.202102987.

[17] S. Brittman and E. C. Garnett, "Measuring n and k at the microscale in single crystals of $CH_3NH_3PbBr_3$ perovskite," *J. Phys. Chem. C*, vol. 120, no. 1, pp. 616–620, Jan. 2016, doi: 10.1021/acs.jpcc.5b11075.

[18] J.-S. Park *et al.*, "Electronic structure and optical properties of α-$CH_3NH_3PbBr_3$ perovskite single crystal," *J. Phys. Chem. Lett.*, vol. 6, no. 21, pp. 4304–4308, Oct. 2015, doi: 10.1021/acs.jpclett.5b01699.

[19] Y. Wang, L. Zhu, and C. Du, "Polarization-sensitive light sensors based on a bulk perovskite $MAPbBr_3$ single crystal," *Materials*, vol. 14, no. 5, p. 1238, Mar. 2021, doi: 10.3390/MA14051238.

[20] Y. Yang, M. Yang, Z. Li, R. Crisp, K. Zhu, and M. C. Beard, "Comparison of recombination dynamics in $CH_3NH_3PbBr_3$ and $CH_3NH_3PbI_3$ perovskite films: Influence of exciton binding energy," *J. Phys. Chem. Lett.*, vol. 6, no. 23, pp. 4688–4692, Nov. 2015, doi: 10.1021/acs.jpclett.5b02290.

[21] N. Sestu *et al.*, "Absorption f-sum rule for the exciton binding energy in methylammonium lead halide perovskites," *J. Phys. Chem. Lett.*, vol. 6, no. 22, pp. 4566–4572, Nov. 2015, doi: 10.1021/acs.jpclett.5b02099.

[22] X. Ziang, "Refractive index and extinction coefficient of $CH_3NH_3PbI_3$ studied by spectroscopic ellipsometry," *Opt. Mater. Exp.*, vol. 5, no. 1, pp. 29–43, Jan. 2015, doi: 10.1364/OME.5.000029.

[23] L. Fu, H. Li, L. Wang, R. Yin, B. Li, and L. Yin, "Defect passivation strategies in perovskites for an enhanced photovoltaic performance," *Energy Environ. Sci.*, vol. 13, no. 11, pp. 4017–4056, Nov. 2020, doi: 10.1039/D0EE01767A.

[24] J. A. Geurst, "Theory of space-charge-limited currents in thin semiconductor layers," *Phys. Status Solidi B*, vol. 15, no. 1, pp. 107–118, 1966, doi: 10.1002/PSSB.19660150108.

[25] R. Zuleeg and P. Knoll, "Space-charge-limited currents in heteroepitaxial films of silicon grown on sapphire," *Appl. Phys. Lett.*, vol. 11, no. 6, pp. 183–185, Sep. 1967, doi: 10.1063/1.1755088.

[26] N. Lu, D. Wang, M. Han, B. Zhao, G. Wu, and Z. Hu, "Growth of two-dimensional formamidine lead halide perovskite single-crystalline sheets and their optoelectronic properties," *Chem. Commun.*, vol. 57, no. 15, pp. 1939–1942, Feb. 2021, doi: 10.1039/D0CC06957D.

[27] T. Liu, W. Tang, S. Luong, and O. Fenwick, "High charge carrier mobility in solution processed one-dimensional lead halide perovskite single crystals and their application as photodetectors," *Nanoscale*, vol. 12, no. 17, pp. 9688–9695, May 2020, doi: 10.1039/D0NR01495H.

[28] M. I. Saidaminov *et al.*, "Planar-integrated single-crystalline perovskite photodetectors," *Nature Commun.*, vol. 6, no. 1, pp. 1–7, Nov. 2015, doi: 10.1038/NCOMMS9724.

[29] J. N. Fru, N. Nombona, and M. Diale, "Synthesis and characterisation of methylammonium lead tri-bromide perovskites thin films by sequential physical vapor deposition," *Phys. B, Condens. Matter*, vol. 578, Feb. 2020, Art. no. 411884, doi: 10.1016/j.physb.2019.411884.

[30] H. Arora *et al.*, "Demonstration of a broadband photodetector based on a two-dimensional metal–organic framework," *Adv. Mater.*, vol. 32, no. 9, Jan. 2020, Art. no. 1907063, doi: 10.1002/ADMA.201907063.

[31] Y. Li *et al.*, "High-performance perovskite photodetectors based on solution-processed all-inorganic $CsPbBr_3$ thin films," *J. Mater. Chem. C*, vol. 5, no. 33, pp. 8355–8360, 2017, doi: 10.1039/C7TC02137B.

[32] L. Li, S. Ye, J. Qu, F. Zhou, J. Song, and G. Shen, "Recent advances in perovskite photodetectors for image sensing," *Small*, vol. 17, no. 18, Mar. 2021, Art. no. 2005606, doi: 10.1002/SMLL.202005606.

[33] X. Geng *et al.*, "Ultrafast photodetector by integrating perovskite directly on silicon wafer," *ACS Nano*, vol. 14, no. 3, pp. 2860–2868, Feb. 2020, doi: 10.1021/acsnano.9b06345.

[34] C. Liu, Q. Tai, N. Wang, G. Tang, H. Loi, and F. Yan, "Sn-based perovskite for highly sensitive photodetectors," *Adv. Sci.*, vol. 6, no. 17, Jul. 2019, Art. no. 1900751, doi: 10.1002/ADVS.201900751.

[35] A. Afal, S. Coskun, and H. E. Unalan, "All solution processed, nanowire enhanced ultraviolet photodetectors," *Appl. Phys. Lett.*, vol. 102, no. 4, Jan. 2013, Art. no. 043503, doi: 10.1063/1.4789757.

[36] F. Abbasi, F. Zahedi, and M. H. Yousefi, "Performance improvement of UV photodetectors using Cd-doped ZnO nanostructures," *J. Mater. Sci., Mater. Electron.*, vol. 32, no. 14, pp. 19614–19625, Jul. 2021, doi: 10.1007/S10854-021-06482-5.

[37] R. S. Veerla, P. Sahatiya, and S. Badhulika, "Fabrication of a flexible UV photodetector and disposable photoresponsive uric acid sensor by direct writing of ZnO pencil on paper," *J. Mater. Chem. C.*, vol. 5, no. 39, pp. 10231–10240, Jul. 2017, doi: 10.1039/C7TC03292G.

[38] Y. Gao *et al.*, "TiO_2 nanorod arrays based self-powered UV photodetector: Heterojunction with NiO nanoflakes and enhanced UV photoresponse," *ACS Appl. Mater. Interface*, vol. 10, no. 13, pp. 11269–11279, Mar. 2018, doi: 10.1021/acsami.7b18815.

[39] Z. Wang *et al.*, "Transferable and flexible nanorod-assembled TiO_2 cloths for dye-sensitized solar cells, photodetectors, and photocatalysts," *ACS Nano*, vol. 5, no. 10, pp. 8412–8419, Sep. 2011, doi: 10.1021/NN203315K.

[40] D.-Y. Zhang, C.-W. Ge, J.-Z. Wang, T.-F. Zhang, Y.-C. Wu, and F.-X. Liang, "Single-layer graphene-TiO_2 nanotubes array heterojunction for ultraviolet photodetector application," *Appl. Surf. Sci.*, vol. 387, pp. 1162–1168, Nov. 2016, doi: 10.1016/j.apsusc.2016.07.041.

[41] B. Butun, T. Tut, E. Ulker, T. Yelboga, and E. Ozbay, "High-performance visible-blind GaN-based p-i-n photodetectors," *Appl. Phys. Lett.*, vol. 92, no. 3, Jan. 2008, Art. no. 033507, doi: 10.1063/1.2837645.

[42] A. Gundimeda *et al.*, "Fabrication of non-polar GaN based highly responsive and fast UV photodetector," *Appl. Phys. Lett.*, vol. 110, no. 10, Mar. 2017, Art. no. 103507, doi: 10.1063/1.4978427.

[43] W. C. Lien, D. S. Tsai, D. H. Lien, D. G. Senesky, and A. P. Pisano, "4H–SiC metal–semiconductor–metal ultraviolet photodetectors in operation of 450 °C," *IEEE Electron Device Lett.*, vol. 33, no. 11, Oct. 2012, pp. 1586–1588, doi: 10.1109/LED.2012.2214759.

[44] M. A. Yildirim and K. Teker, "Self-powered fine-pattern flexible SiC single nanowire ultraviolet photodetector," *J. Alloys Compounds*, vol. 868, Jul. 2021, Art. no. 159255, doi: 10.1016/j.jallcom.2021.159255.

[45] R. McClintock *et al.*, "High quantum efficiency AlGaN solar-blind p-i-n photodiodes," *Appl. Phys. Lett.*, vol. 84, no. 8, pp. 1248–1250, Feb. 2004, doi: 10.1063/1.1650550.

[46] A. Kalra, S. Rathkanthiwar, R. Muralidharan, S. Raghavan, and D. N. Nath, "Polarization-graded AlGaN solar-blind p-i-n detector with 92% zero-bias external quantum efficiency," *IEEE Photon. Technol. Lett.*, vol. 31, no. 15, pp. 1237–1240, Aug. 1, 2019, doi: 10.1109/LPT.2019.2923147.